

## Flow Response to Periodic Heating and Cooling in a Reservoir

Chengwang Lei, John C. Patterson and Yong Sha

School of Engineering, James Cook University,  
Townsville, QLD 4811, AUSTRALIA

### Abstract

An unsteady model is formed and solved numerically in order to investigate the transient circulations in a reservoir subject to periodic heating and cooling. The numerical results reveal that there is a time lag in the response of the overall flow to the switch of the thermal forcing, and thermal instabilities play an important role in breaking the residual circulation and reversing the flow in deep waters.

### Introduction

Large-scale convective circulations in response to the transient daytime heating and night-time cooling take place in the sidearm of reservoirs or shallow littoral waters with gently sloped bottoms. These convective circulations greatly influence the transport of nutrients and pollutants between the shallow region and the bulk deep water [1, 2]. When the shallow and deep regions are exposed to a uniform rate of surface cooling under the night-time condition, the shallow water cools faster than the deep water. The difference in the cooling rate then results in a horizontal temperature gradient which in turn drives a downward dense gravity current along the sloping bottom [2, 3]. A similar but converse statement can be made for the daytime heating condition [1, 4, 5].

In general the flow response in reservoirs is characterized by unsteady forcing and large scale circulations in field situations. Of particular interest is the response of the convective circulation to the switch between the daytime heating and night-time cooling. This will be the major focus of this paper.

### Model Formulation and Normalisation

A two-dimensional (2D) reservoir model consisting of a region with a sloping bottom and another region of a uniform water depth is considered here (see figure 1). Here,  $h$  is the maximum water depth in the reservoir. Previous investigations suggested that 2D numerical models can reproduce major flow features observed in both heating and cooling experiments [5, 6].

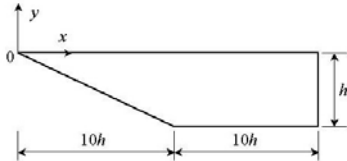


Figure 1 Sketch of the flow domain and coordinate system.

Two types of thermal forcing are constructed for the reservoir model in order to simulate the diurnal cycle in field situations. Assume the period of the thermal forcing is  $P$ . During the first half of every forcing cycle, solar radiation with a time-dependent intensity of  $I_0 \sin(2\pi t/P)$  is imposed at the water surface. Here  $I_0$  is the maximum intensity of the solar radiation at the water surface and  $t$  is the time. The solar radiation entering from the water surface is absorbed by the water body according to the Beer's law:

$$I = I_0 e^{-\eta y} \sin(2\pi t/P) \quad (y \leq 0) \quad (1)$$

where  $I$  is the radiation intensity at a given water depth ( $-y$ ), and  $\eta$  is the attenuation coefficient of water. The attenuation

coefficient can be regarded as a constant [4, 5]. It is assumed in this study that any radiation reaching the bottom is fully absorbed by the bottom and the absorbed energy is then released back into the water as a boundary heat flux. Moreover, it is assumed that the heat loss through the water surface during the heating phase is negligible, and all the radiation entering through the water surface is ultimately absorbed by the water.

During the second half of the forcing cycle, heat is lost through the water surface, and an unsteady heat flux  $H$  defined below is imposed uniformly across the water surface:

$$H = H_0 \sin(2\pi t/P) \quad (2)$$

where  $H_0$  is the maximum heat flux during the cooling period. The construction of the heating and cooling conditions through the water surface ensures a smooth transition from one type of forcing to the other, and the combination of these two types of thermal forcing allows us to simulate an entire diurnal cycle. Moreover, it is assumed that the heat absorbed by the water body during the heating phase is in a balance with the heat released by the water body during the cooling phase, and thus  $H_0 = I_0$ .

The evolutions of flow and temperature in the reservoir are governed by the Navier-Stokes and energy equations as follows:

$$u_x + v_y = 0 \quad (3)$$

$$u_t + uu_x + vv_y = -\rho_0^{-1} p_x + \nu \nabla^2 u \quad (4)$$

$$v_t + uv_x + vv_y = -\rho_0^{-1} p_y + \nu \nabla^2 v + g\beta(T - T_0) \quad (5)$$

$$T_t + uT_x + vT_y = \alpha \nabla^2 T + Sr \quad (6)$$

where  $u$  and  $v$  are the velocity components along  $x$  and  $y$  direction respectively,  $p$  the pressure,  $T$  the temperature,  $\rho_0$  the density at the reference temperature  $T_0$ ,  $g$  the acceleration due to gravity,  $\nu$  kinematic viscosity,  $\alpha$  the thermal diffusivity, and  $\beta$  the thermal expansion coefficient.  $Sr$  is the internal heat source term quantifying the radiation absorption by the water body under the daytime condition, and it is set to zero for the night-time cooling period. Thus,

$$Sr = \begin{cases} \frac{I_0}{\rho_0 C_p} \eta e^{-\eta y} \sin(2\pi t/P) & \text{if } \sin(2\pi t/P) \geq 0 \\ 0 & \text{if } \sin(2\pi t/P) < 0 \end{cases} \quad (7)$$

where  $C_p$  is the specific heat of water.

The governing equations are subject to the following initial and boundary conditions:

- (1) At  $t = 0$ ,  $u = v = 0$ ,  $T = T_0$ .
- (2) At the deep end ( $x = 20h$ ), an insulated and rigid non-slip boundary condition applies, i.e.  $u = v = 0$ , and  $T_x = 0$ .
- (3) The water surface ( $y = 0$ ) is assumed to be stress-free ( $v = 0$  and  $u_y = 0$ ). The thermal boundary condition is given by

$$-k \frac{\partial T}{\partial y} = \begin{cases} 0 & \text{if } \sin(2\pi t/P) \geq 0 \\ -H_0 \sin(2\pi t/P) & \text{if } \sin(2\pi t/P) < 0 \end{cases} \quad (8)$$

where  $k$  is the thermal conductivity.

- (4) The sloping and horizontal bottom is rigid and non-slip ( $u = v = 0$ ). The thermal boundary condition is given by

$$-k \frac{\partial T}{\partial n} = \begin{cases} I_0 e^{\gamma n} \sin(2\pi t/P) & \text{if } \sin(2\pi t/P) \geq 0 \\ 0 & \text{if } \sin(2\pi t/P) < 0 \end{cases} \quad (9)$$

where  $n$  is the direction normal to the bottom.

In this study, the governing equations are normalized using the following scales:

Length ( $x, y$ ):	$\sim h$ ;
Velocity ( $u, v$ ):	$\sim \alpha/h$ ;
Time ( $t, P$ ):	$\sim h^2/\alpha$ ;
Temperature variation ( $T - T_0$ ):	$\sim I_0 h/k$ ;
Pressure gradient ( $p_x, p_y$ ):	$\sim \rho_0 g \beta I_0 h/k$ ;
Attenuation coefficient ( $\eta$ ):	$\sim 1/h$ .

The normalised governing equations are rewritten as:

$$u_x + v_y = 0 \quad (10)$$

$$u_t + u u_x + v v_y = -(Pr^2 Gr) p_x + Pr \nabla^2 u \quad (11)$$

$$v_t + u v_x + v v_y = -(Pr^2 Gr) p_y + Pr \nabla^2 v + (Pr^2 Gr) T \quad (12)$$

$$T_t + u T_x + v T_y = \nabla^2 T + Sr \quad (13)$$

where the Grashof ( $Gr$ ) and Prandtl ( $Pr$ ) numbers are defined as:

$$Gr = \frac{g \beta I_0 h^4}{\nu^2 k} \quad \text{and} \quad Pr = \frac{\nu}{\alpha}, \quad (14)$$

and the source term is given by

$$Sr = \begin{cases} \eta e^{\gamma n} \sin(2\pi t/P) & \text{if } \sin(2\pi t/P) \geq 0 \\ 0 & \text{if } \sin(2\pi t/P) < 0 \end{cases} \quad (15)$$

All the variables in equations (10) ~ (15) are now dimensionless. The initial and boundary conditions are also normalised accordingly. For brevity, details are not given here.

### Numerical Considerations

The normalised governing equations are solved using a finite difference scheme. Standard second-order central differencing is used for all spatial derivatives except the non-linear terms in the momentum and energy equations, which are approximated with a modified second-order upwind scheme. The time integration for the velocity components and temperature is by a second-order time accurate backward differencing scheme. Details of the numerical schemes can be found in [4].

Since the present investigation is relevant to reservoirs or lakes with water as the medium, the Prandtl number is fixed at 7. The numerical simulations are based on a laboratory scaled model with a maximum water depth of 0.1 m and a bottom slope of 0.1 in the sloping region. Consider a peak intensity of 50 W/m<sup>2</sup> for the thermal forcing with a cycle period of approximately 4 hours. The corresponding dimensionless period of forcing is set to 0.2, and the Grashof number is calculated to be  $1.73 \times 10^7$  based on a room temperature of 20°C. The dimensionless attenuation coefficient is set to 0.62 according to the experimental measurement reported in [5]. A less-than-unity value for the dimensionless attenuation coefficient implies that the maximum water depth is less than the penetration length scale of the radiation, and thus a significant portion of the radiation entering through the water surface will penetrate all the way through the water depth and reach the bottom. For the purpose of examining the dependence of the flow response on the Grashof number, another case with  $Gr = 10^6$  is also calculated.

The results presented here were obtained using a non-uniform mesh of  $201 \times 61$  and a time step of  $10^{-6}$ . In order to test the dependence of numerical solutions on the grid resolution, a coarser mesh of  $121 \times 61$  and a finer mesh of  $301 \times 91$  are also adopted to calculate the case with the higher Grashof number. It

is found that all three meshes gave similar results in terms of the overall response of the flow to the periodic forcing.

For the discussion of the numerical results, a horizontal volumetric flow rate is defined in a 2D domain as [4]

$$Q(x) = 0.5 \int_{-h_x}^0 |u| dy, \quad (16)$$

where  $h_x$  is the local water depth.  $Q(x)$  quantifies the intensity of the horizontal exchange flow at a given  $x$  location. Here, the dimensional quantity has been normalised using the scales  $Q \sim \alpha$ . By integrating  $Q(x)$  along the horizontal direction as follows:

$$\bar{Q} = L^{-1} \int_0^L Q(x) dx, \quad (17)$$

an averaged volumetric flow rate  $\bar{Q}$  is obtained. Here,  $L$  is the total length of the domain.

### Flow Response to Periodic Forcing

The numerical results obtained for  $Gr = 1.73 \times 10^7$  are reported here. The simulation covers 10 full thermal forcing cycles in order to minimize the effect of the start-up flow, and the results of the last cycle are presented. In this paper, we only examine the flow response to the daytime heating process corresponding to the first-half of the forcing cycle. Figure 2 plots the temperature contours at representative time instances, and Figure 3 plots the corresponding streamlines. The times indicated in these two figures are relative to the end of the ninth or the beginning of the tenth forcing cycle ( $t = 9P$ ).

At the beginning of this cycle ( $t = 0.00P$ ), the surface cooling is switched off and the radiation heating is switched on at the same time. However, residual temperature and flow structures formed in the previous cooling phase are still present. Figure 2(a) clearly shows that a cold gravity current is flowing downward along the sloping bottom and into the main water body along the flat bottom. The downwelling gravity current is a major feature expected in coastal waters during the night-time cooling process. Corresponding to this downwelling flow, a cavity-wide large-scale circulation is present, as can be seen in figure 3(a). Here the solid streamlines indicate a counter-clockwise circulation. Conversely, dashed streamlines indicate a clockwise circulation (see for example figures 3b, 3c). It is also seen in figure 3(a) that the cavity-wide circulation has multiple cores, indicating the residual effect of plunging plumes formed during cooling.

As the radiative heating intensifies, the water temperature across the entire domain increases as a consequence of the absorption of radiation entering from the water surface. Of particular interest is the growth of a thermal boundary layer along the sloping and flat bottom (see figure 2b). The thermal boundary layer forms because, in shallow waters, a significant portion of the radiation reaches the bottom (the so-called residual radiation) and is absorbed by the bottom. The absorbed energy is then re-emitted back into the water through a boundary heat flux. The combined effects of the bottom boundary heat flux and the topography in the sloping region result in an upward flow along the slope [4, 5], as indicated by the dashed lines in figure 3(b). This upwelling flow is in the opposing direction to the residual flow formed during the previous cooling phase. It is seen in figure 3(b) that, at this time, the reverse flow appears only in the region near the tip and the slope. In the region with a flat bottom, the bottom boundary heat flux does not produce any flow at this stage due to the absence of the topographical effect.

Further to the previous description, the thermal boundary layer continues to grow (figure 2c), and the region with the reverse flow expands toward the core (figure 3c). At this time ( $t = 0.07P$ ), the flow in the region above the slope is almost reversed completely, and the residual flow has been pushed toward the

deep-end wall. It is worth noting that the thermal boundary layer is stable until this time.

As the thermal boundary layer grows further, it eventually becomes unstable to the Rayleigh-Benard type instabilities. As a consequence, rising hot-water plumes occur all the way along the bottom thermal boundary layer, as can be seen in [figure 2\(d\)](#). The thermal instability in the form of rising plumes is the same as the instability observed in shallow waters under constant radiative heating [4, 5]. As the hot-water plumes move upward, they generate secondary flows by pushing and entraining the nearby fluid. The rising thermals also break up the residual circulation and form a cellular flow structure in the domain (see [figure 3d](#)).

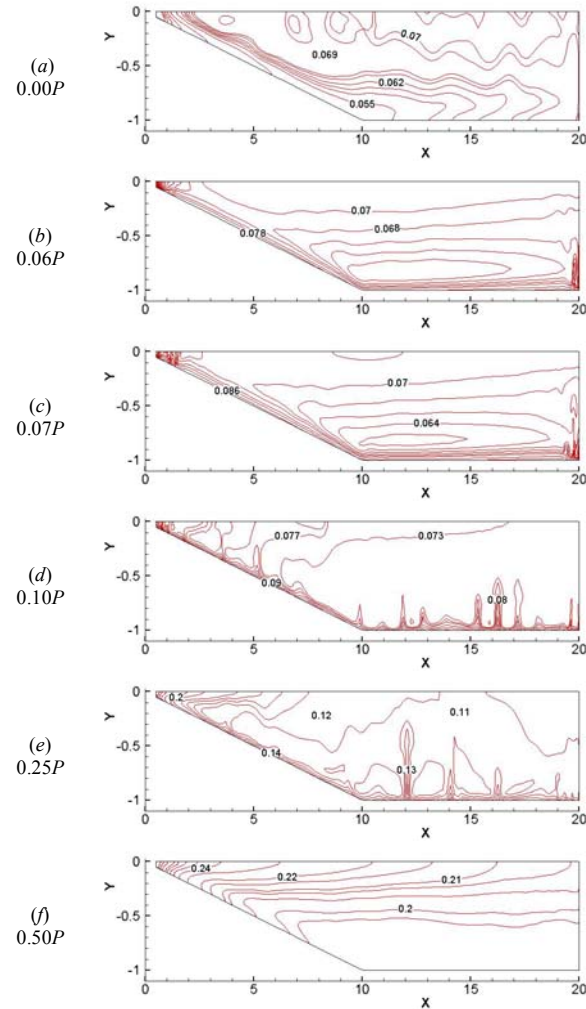


Figure 2 Temperature contours at different stages of the flow response to radiative heating ( $Gr = 1.73 \times 10^7$ ).

The subsequent flow response in the domain is dominated by the occurrence of the thermal instability. [Figure 2\(e\)](#) plots the temperature contours at  $t = 0.25P$  when the intensity of the radiative heating peaks, and [figure 3\(e\)](#) plots the corresponding streamlines. The occurrence of the rising thermals is clearly seen in [figure 2\(e\)](#), and accordingly, the cellular flow structure persists (see [figure 3e](#)). Another effect of the thermal instability in the form of rising thermals is to accelerate the vertical mixing in the domain, which in turn reduces the temperature gradient over the local water depth and tends to weaken the thermal instability.

After the time  $t = 0.25P$ , the intensity of the radiative heating starts to decline. However, it is observed that the bottom boundary heating mechanism discussed above, along with the

associated thermal layer instability and the resulting cellular flow structure, persists for a relatively long time. Eventually, the thermal instability dies out when the radiation entering from the water surface becomes very weak. At this stage, the flow response is dominated by the topographic effect in the sloping region. Since the radiation entering from the surface is uniform across the length of the domain, but the water depth increases gradually in the sloping region, the averaged absorption of the radiation over the local water depth increases toward the tip. Therefore, a horizontal temperature gradient is established in the domain, which drives a cavity-wide circulation up the slope and out of the tip region along the surface. The representative temperature and flow structures at this stage is shown in [figures 2\(f\) and 3\(f\)](#), which plot the contours of temperature and streamlines at  $t = 0.50P$ . Clearly, a temperature gradient exists along the slope and the water surface, and in the majority of the core region, the water is stably stratified (refer to [figure 2f](#)). The corresponding streamlines indicate a clockwise circulation across the entire domain (see [figure 3f](#)).

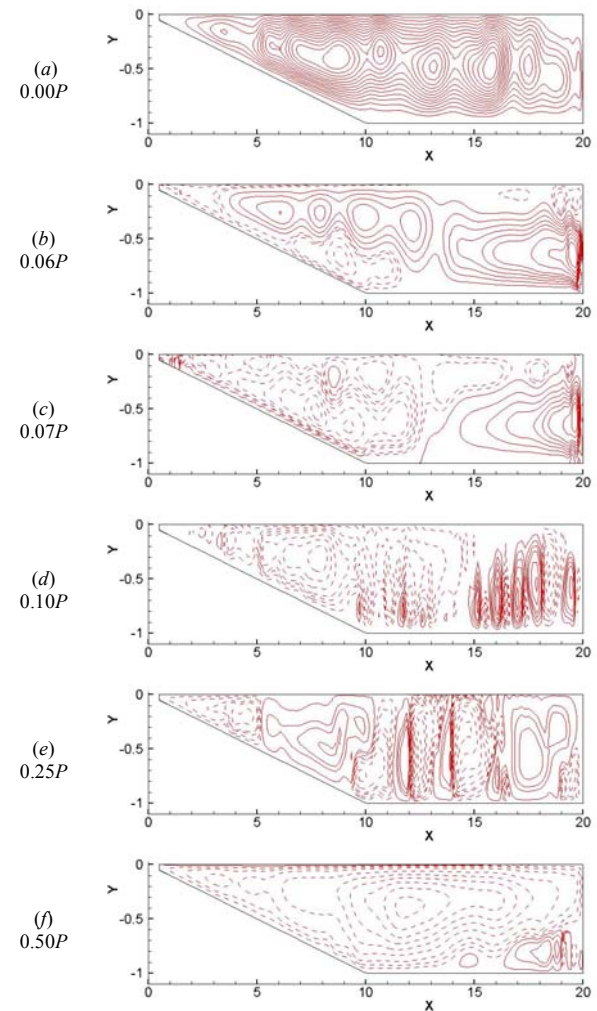


Figure 3 Streamlines at different stages of the flow response to radiative heating ( $Gr = 1.73 \times 10^7$ ).

The temperature and flow structures shown in [figures 2\(f\) and 3\(f\)](#) respectively also represent the residual structures from the daytime heating phase since the radiative heating is switched off and at the same time the surface cooling is switched on at  $t = 0.50P$ . The flow response during the second-half of the forcing cycle ( $0.50P < t < P$ ) may be described in a similar way. For brevity, the detailed description is not included here. In general,

the flow response during the surface cooling phase is very similar to the radiative heating phase. The major difference between the heating and cooling phases is that there is no thermal boundary layer growing along the bottom. Instead, a thermal boundary layer grows underneath the water surface. It is this surface layer that eventually becomes unstable, and the thermal instability in the form of sinking cold-water plumes breaks the residual circulation and promotes vertical mixing. At the end of the cooling phase, temperature and flow structures identical to those shown in figures 2(a) and 3(a) are formed, and the previously described flow response is repeated in the following cycle.

### Time History of Horizontal Exchange Flowrate

Features of the flow response to the diurnal forcing can also be observed from the time history of the horizontal exchange flowrate, which is presented in figure 4 for two different Grashof numbers along with the corresponding thermal forcing. A positive value of the thermal forcing in figure 4(a) represents the daytime radiative heating, whereas a negative value represents the night-time surface cooling. In figure 4,  $t = 1$  is the beginning of the sixth cycle, and  $t = 2$  is the end of the tenth cycle. At  $t = 1$ , the thermal forcing is switching from the night-time cooling to the daytime heating, and since then, the intensity of the radiative heating increases for a quarter of the cycle.

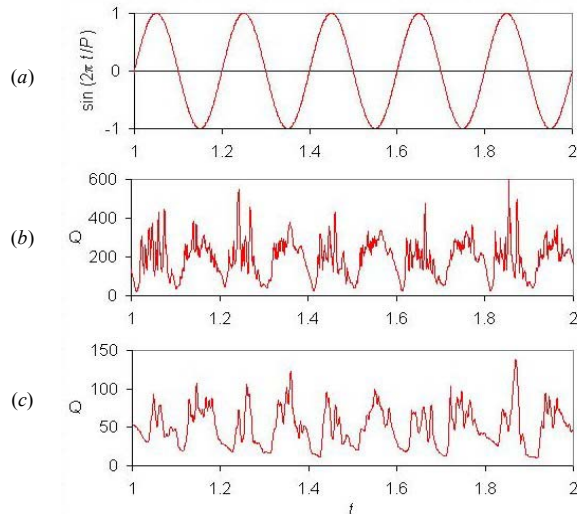


Figure 4. Time history of (a) the thermal forcing; (b) the averaged horizontal exchange flowrate for  $Gr = 1.73 \times 10^7$ ; (c) the averaged horizontal exchange flowrate for  $Gr = 10^6$ .

Consider first the case with  $Gr = 1.73 \times 10^7$  shown in figure 4(b). It is seen in this figure that, in contrast to the increasing thermal forcing, the averaged horizontal flowrate decreases from  $t = 1$  until  $t = 1.012$ . This is due to the effect of the residual circulation formed in the precedent cooling phase. After  $t = 1.012$ , the averaged horizontal flowrate starts to increase, which is in phase with the thermal forcing. The above observation indicates that the lag time of the flow response to the switch of the thermal forcing from cooling to heating is approximately 6% of the forcing period ( $P = 0.2$ ). As the radiative heating intensifies, thermal instabilities associated with the bottom heating start to occur, which cause the fluctuations of the horizontal exchange flowrate. It is seen in figure 4(b) that the thermal instabilities dominate most of the heating phase and persists until well after the radiative heating peaks. When the radiative heating becomes sufficiently weak, the thermal instability dies out, and the overall flowrate decreases until a certain time after the cooling phase

starts. Similarly, there is a lag of the reversal of the overall flow relative to the switch of the thermal forcing from heating to cooling, and the thermal instabilities dominate the flow response for most of the cooling phase.

It is also noticeable in figure 4(b) that the overall strength of the circulation in the heating phase is relatively weaker than that in the cooling phase although the imposed surface heat fluxes are of equal amounts. This is because part of the radiation entering from the water surface is absorbed by the water body, which results a stable stratification in the reservoir.

The time history of the averaged horizontal exchange flowrate obtained for  $Gr = 10^6$  (see figure 4(c)) exhibits similar features. However, three additional features in comparison with the higher Grashof number case are worth noting. First, the strength of the overall circulation is much weaker than the previous case. Second, the thermal instability becomes weaker, and the frequency is also reduced at  $Gr = 10^6$ , as shown in figure 4(c). Finally, the lag time of the flow response to the switch of the thermal forcing is longer for the lower Grashof number case. The lag time for the switch from cooling to heating is estimated to be about 17% of the forcing period for  $Gr = 10^6$ .

### Summary

The flow response to diurnal thermal forcing in shallow waters is described based on numerical simulations. It is observed that there is a time lag of the flow response to the switch of the thermal forcing from surface cooling to radiative heating. The lag time estimated in the present study is significantly shorter than that reported in [1] and in field situations. This is mainly attributed to the shallow water assumption in the present investigation. The flow response in deep waters with a water depth beyond the penetration length scale of the radiation is worth investigating.

It is also observed that the thermal instabilities associated with the bottom heating during the daytime phase and the surface cooling during the night-time phase play an important role in breaking the residual circulation and reversing the flow in deep waters. These instabilities are also the dominant mechanism responsible for the vertical mixing in field situations.

### Acknowledgement

This research was supported by the Australian Research Council and the Australian Partnership for Advanced Computing.

### References

- [1] Farrow D.E., Periodically forced natural convection over slowly varying topography, *J. Fluid Mech.*, **508**, 2004, 1–21.
- [2] Sturman J. J., Oldham C. E. & Ivey G. N., Steady convective exchange flows down slopes, *Aquat. Sci.*, **61**, 1999, 260–278.
- [3] Horsch G.M. & Stefan H.G., Convective circulation in littoral water due to surface cooling, *Limn. Ocean.*, **33**, 1988, 1068–1083.
- [4] Lei C. & Patterson J.C., Unsteady natural convection in a triangular enclosure induced by absorption of radiation, *J. Fluid Mech.*, **460**, 2002, 181–209.
- [5] Lei C. & Patterson J.C., A direct three-dimensional simulation of radiation-induced natural convection in a shallow wedge, *Intl J. Heat Mass Transfer*, **46**, 2003, 1183–1197.
- [6] Horsch G.M., Stefan H.G. & Gavali S., Numerical simulation of cooling-induced convective currents on a littoral slope, *Intl J. Num. Meth. Fluids*, **19**, 1994, 105–134.